Soft Matter

Mapping Amyloid-β(16 22) Nucleation Pathways using Fluorescence Lifetime Imaging Microscopy

Journal:	*Soft Matter*
Manuscript ID:	SM-ART-02-2014-000361.R1
Article Type:	Paper
Date Submitted by the Author:	01-Apr-2014
Complete List of Authors:	Anthony, Neil; Emory University, Department of Physics Mehta, Anil; Emory University, Departments of Chemistry and Biology Lynn, David; Emory University, Departments of Chemistry and Biology Berland, Keith; Emory University, Department of Physics

Mapping Amyloid-β(16-22) Nucleation Pathways using Fluorescence Lifetime Imaging Microscopy

Neil R. Anthony[a], *Anil K. Mehta*[b], *David G. Lynn*[b], *and Keith M. Berland*[a]

[a] Department of Physics, Emory University, Atlanta, GA

[b] Departments of Chemistry and Biology, Emory University, Atlanta, GA

Abstract

The cross-β peptide phase is associated with numerous functional biomaterials and deleterious disease related aggregates. While these diverse and ubiquitous paracrystalline assemblies have been widely studied, a fundamental understanding of the nucleation and aggregation pathways to these structures remains elusive. Here we highlight a novel application of fluorescence lifetime imaging microscopy in characterising the critical stages of peptide aggregation. Using the central nucleating core of the amyloid-ß (Aß), Aß(16-22), as a model cross-ß system, and utilising a small fraction of rhodamine labelled peptide, Rh110-Aß(17-22), we map out a folding pathway from monomer to paracrystalline nanotube. Using this intrinsic fluorescence reporter, we demonstrate the effects of interfaces and evaporation on the nucleation of sub-critical concentration solutions, providing access to previously uncharacterised intermediate morphologies. Using fluorescence lifetime, we follow the local peptide environment through the stages of nucleation and hydrophobic collapse, ending in a stable final structure. This work demonstrates that the lifetime of fluorescent reporters provides a valuable metric for investigating dynamic processes and structural pathways in amyloid nucleation and maturation.

Introduction

Investigations of the protein aggregates associated with neurodegenerative diseases have continued to highlight the increasingly urgent need for better treatments [1]. Given the pathology of the disease, such treatments are tied to a better understanding of the complex landscape of biopolymer folding, specifically protein misfolding events [2-5]. Transient soluble molten globule monomers and dynamic oligomers are central to both folding and misfolding, and the intermolecular phases may provide critical on- and off-pathway intermediates in the formation of the β-sheet rich peptide phases that appear to be central to the etiology of dementia and cellular toxicity [4, 6-14]. Understanding the subtleties of the inter- and intra-molecular peptide interactions that determine protein aggregation is thus vital for a pathogenic understanding leading to the development of therapeutic strategies.

Hydrophobically-driven peptide collapse creates a reduced dielectric environment critical for intra-molecular peptide assembly [15-19]. These dynamic intermolecular aggregates have been predicted in numerous protein aggregation simulations [20-23] and observed experimentally [24-27]. Nucleating seeds capable of templating elongation and growth have also been observed once a critical concentration

(CC) of peptide has been achieved [28], together with a lag-phase that typically precedes amyloid growth [29, 30]. In addition, air-water-interfaces (AWIs) have been shown to accelerate the nucleation process, both in deleterious protein aggregation [31-33] and functional bio-aggregates [34-36]. The heterogeneous environment of interfaces can lead to differing aggregate morphology, nucleation pathways, altered membrane interactions, and has been suggested to play a pivotal role in toxicity [37-41].

Surfaces such as AWIs, hydrophobic-hydrophilic interfaces (HHIs), and lipid bilayers and micelles continue to be identified as local environments critical for these phase transitions [31, 33, 42-46]. Nevertheless, capturing nucleation events and nascent growth at the critical soluble pre-fibrillar intermediate stages has proven to be inherently difficult due to their transient nature. Numerous experiments have employed the sensitivity and specificity of fluorescence measurements to assist in identifying transient species [41, 47]. The amyloid specific dye thioflavin-T (ThT) [48] has been used to quantify amyloid formation at AWIs in bulk solution [49], and spatially resolved fibre growth on glass surfaces using total internal reflection microscopy (TIRFM) [39, 50-52]. In addition, TIRFM has been employed to observe 2D diffusion of weakly adsorbed amyloid-β (Aß) peptides, where nucleation is limited to surface adhered peptides [53], highlighting the subtleties of interface characteristics

Here we highlight the role of interfaces as a control mechanism of the initial phase transition crucial to aggregation and the subsequent nucleation events. Using one of the most thoroughly investigated model amyloid systems, Aß(16-22) (see [28] and references therein), we previously followed the initial nucleation stages of cross-β peptide nanotubes utilizing a small fraction (~1%) of rhodamine-labeled peptides [24]. Lys16 of Aß(16-22) was replaced with rhodamine-110 (R110) to produce a positively charged label (denoted Rh17-22) that co-assembled with Aß(16-22) and became incorporated into the final cross-β phase [24]. Aß(16-22) co-assembled with Rh17-22 allowed the dynamic phases present during nucleation to be captured, whereby 'molten globule' aggregates adhered to glass surfaces were directly observed as centres of nucleation and growth of cross-β nanotube structures [24]. Contrary to bound reporters such as ThT, which only discern final structure, the intrinsic nature of the Rh17-22 fluorescence reporter facilitates investigation of intermediate and pre-cross-ß phases in the nucleation pathway.

We demonstrate the effects of AWIs and HHIs on solutions of Aβ(16-22) above and below the peptides critical assembly concentration. The combination of peptide concentrations and a controlled introduction of interfaces allow us to probe the different stages of the nucleation pathways. Specifically, using aeration and vortexing to introduce AWIs and hydrophobic plastic to represent HHIs, we determine that introduced interfaces lead to increased nucleation. This control allows access to previously uncharacterized intermediate morphologies, strongly suspected to be on-pathway seeds to nanotube growth. We also demonstrate that interface effects present during solvent evaporation can also be used to control nucleation, provided the peptide is present during the solvent evaporation. Fluorescence lifetime imaging microscopy (FLIM) reports the nano-scale environment of the intrinsic rhodamine probe within the morphologies accessed utilizing these different interfaces, allowing the nucleation process to be mapped out in terms of known and inferred structures. Further, we expand on previous work by recreating the growing molten globules, and follow the evolution of these aggregates using FLIM to further resolve the fluorescence lifetime of the nucleation events. We have thus followed the morphology and fluorescence lifetime of Aβ(16-22) peptide as it aggregates and forms into paracrystalline cross-β nanotubes. Using numerous interfaces allows for the morphology, environment, and to some degree, structure of Aβ(16-22) to be mapped from monomer to paracrystalline nanotube.

Results

Our previous investigations did not focus on a role for interfaces in the nucleation of Aß(16-22):Rh17-22 nanotubes [24], yet due to the increased reports of sensitivity to interfaces [31, 33, 42-46], and our continued discoveries, their investigation became more important. Accordingly, 0.5 mM Aβ(16-22)/Rh17-22 (250:1) dissolved in 40% aqueous MeCN pH 2 was loaded twice onto a microscope slide and sealed with coverslip glass (see ref [24]; Figure 1a). During loading, the solvent spreads out across the glass (Figure 1a; frame 1-3), dramatically increasing the air and glass surface interactions available to the peptide solution, while the evaporation of solvents increases concentration and decreases the solubility. As seen previously [24], growth originates from numerous molten assemblies on the glass surface, here shown after ~24 hrs (Figure 1b). Nascent growth from molten globules often exhibits a shorter persistence length than fully mature nanotubes, forming a somewhat meshed network between growing centres. Conversely, the

same sample loaded into the thin gap of a pre-set slide/coverslip vessel using capillary action eliminates both evaporation and the air-solution interface. In contrast to the air-loaded solutions, no significant nucleation could be detected over the same period (
Figure 1c), with only small aggregate spots detected on the glass surfaces, appearing to form at local impurities.

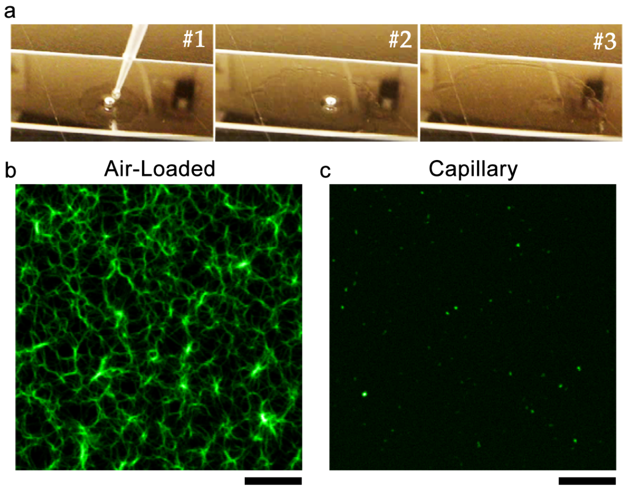

Figure 1 – Role of air water interface (AWI) in sample loading. The air-loaded protocol (a) of adding a drop of 0.5 mM Aß(16-22)/Rh17-22 (250:1) is repeated twice before covering with a cover slip. After ~24 hrs, the air-loaded mixtures produce nucleating aggregates at the glass surface (b). Loading by capillary action on a pre-set slide/coverslip vessel only small aggregates are seen on the glass (c). Scale bar 10 µm.

Evaporation and the presence of AWIs are the two key differences in the above loading protocols. Thus, to further investigate the role of these factors in inducing nucleation we explored the influence of introducing AWIs or solvent evaporation to bulk sample aliquots of 0.04 mM Aß(16-22)/Rh17-22 (200:1) in 40% MeCN pH 2 aqueous solution. The critical concentration (CC) for this batch of Aß(16-22) peptide was ~0.5 mM (the CC varies depending on the particular synthetic batch), inasmuch as the concentrations of these aliquots were an entire order of magnitude lower than concentration required to nucleate growth under quiescent conditions. AWIs were introduced by bubbling air through the sample using a pipette tip and pipettor over a period of 2 weeks, here referred to as “aeration”. Evaporation occurred with a continuous airflow over the open container in the fume hood. The weight of evaporated solution was monitored to match the weight loss in the aerated solution. Solutions were transferred into chambered cover slides in large volumes so that sample loading would not induce nucleation events. Figure 2 shows fluorescence images of aerated (a) and evaporated (b) Aß(16-22)/Rh17-22 solutions. Both aeration and evaporation lead to nucleation of nanotube morphologies for a sample concentration that would otherwise not have any nucleation under similar conditions. The aerated sample has fewer elongated structures while the evaporated sample contains shorter nanotubes and numerous smaller morphologies, although it becomes difficult to distinguish between aggregate seeds and small nanotube sections below a length of 2-3 µm.

The difference in vapour pressure of MeCN and water may lead to changes in solvent conditions (MeCN percentage) during the aeration and evaporation procedures, potentially impacting peptide solubility. To identify the influence of solubility changes in the nucleation process, we aerated the 40% MeCN solvent following the same protocol before dissolving the Aß(16-22)/Rh17-22 peptide, after which the solution was allowed to sit for a further 2 weeks. This procedure did not lead to nanotube nucleation (Figure 2c), and this result seems to strongly indicate that AWIs introduced *via* bubbling play a specific role in nucleating nanotube formation. Any changes in solvent composition due to evaporation appear insufficient to cause the nucleation observed in the aerated samples. In addition to peptide solubility, the presence of the hydrophobic planar rhodamine molecule may be preferentially sequestered at AWIs forming seeds that harbour nanotube nucleation. To test this possibility, we performed a similar control, in which only the Rh1722 peptide was present in solution as it was aerated, followed by the addition of Aß(16-22). This sample again showed no identifiable nanotube nucleation (Figure 2d). Taken together, these data indicate that either aeration or slow evaporation can dramatically enhance nucleation rates and that this is due to the role of interfaces.

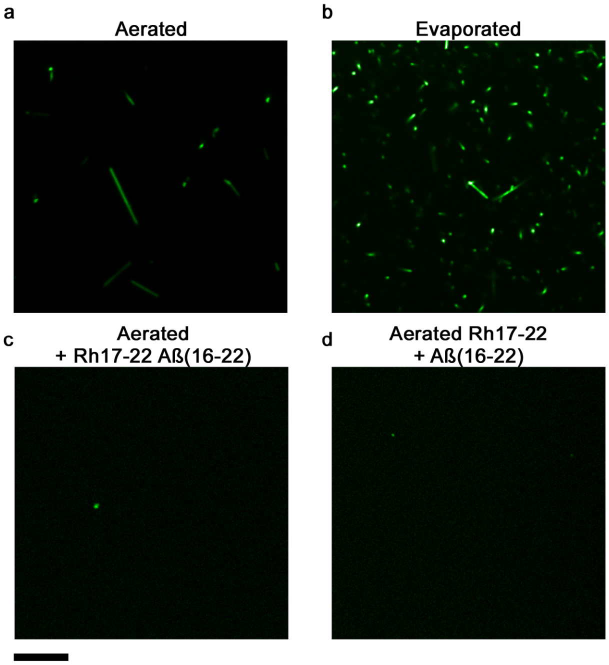

Figure 2 – Comparison of aeration and control evaporations in accessing nucleation events. Aeration of 0.04 mM Aß(16-22)/Rh17-22 (200:1) solutions over a 2 week period (a) produces fewer nanotube structures compared to evaporating to the same change of solution weight (b), yet both processes lead to nanotube formation using a peptide concentration an order of magnitude below the critical concentration. Control evaporation of Rh17-22 in 40% MeCN pH 2 aqueous solution over 2 weeks (c), followed by the addition of Aß(16-22) and a further 2 week incubation time yield no noticeable tube growth. A repeated evaporation control where only the 40% MeCN pH 2 aqueous solution is evaporated prior to peptide addition reveals a similar absence of growth (d). Scale bar 10 µm.

Identifying the role of interfaces enables a degree of experimental control of nucleation events, potentially allowing access to different stages of the nucleation pathway. To demonstrate this, we prepared Aß(16-22) peptide mixtures above and below the critical assembly concentration (CC) and introduced interfaces *via* bubbling or agitation during the initial assembly stages. The CC for this Aß(16-22) peptide batch was independently confirmed to be ~0.35 mM. Aliquots of 0.3 mM and 0.4 mM Aß(16-22)/Rh17-22 mixtures (200:1) were separated and (i) aerated, (ii) vortexed, or (iii) not agitated (quiescent conditions). To attenuate the potential for disrupting the assemblies over time, both aeration and vortexing were performed periodically and with reduced frequency at later stages. Here, to diminish the effects of evaporation, the initial amount of aeration was five times less than above. To provide an additional hydrophobic interface, previously shown to accelerate nucleation [49], we also prepared (iv) a quiescent sample containing a piece of pipette tip. The micro-centrifuge tubes used for assembly were polypropylene and the Eppendorf pipette tip piece used contained anti-static additives designed to increase their hydrophobicity. Under these conditions, the first nanotube morphologies were detected within approximately one week, although the samples were incubated for 1 month before imaging (Figure 3).

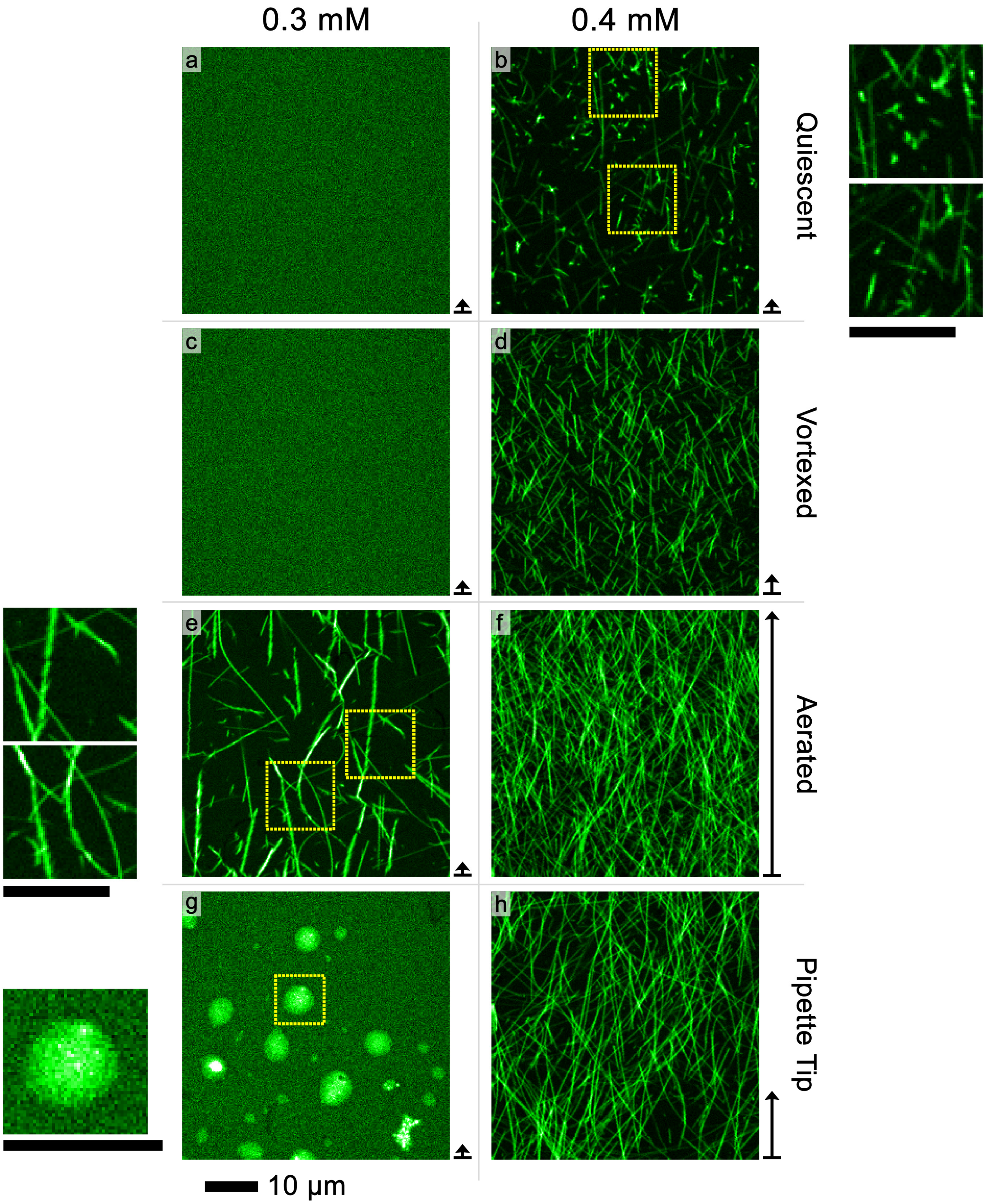

Figure 3 – The effect of interfaces in nucleating assembles. Aß(16-22) solutions below (0.3 mM; left column) and above (0.4 mM; right column) the critical assembly concentration (CC) were allowed to assemble under quiescent conditions, quiescent conditions with permanent hydrophobic-hydrophilic-interface (HHI; pipette tip), periodic vortexing or aeration during the initial assemble period. Each

image is a single ~1 µm thick z-section acquired near the bottom of a chamber box well. Depth indicators at the right hand side of each image denote the approximate height of the nanotube meshed network filling the chamber well, normalized to the depth of the mesh in the 0.4 mM aerated sample which was approximately 20 µm deep. Quiescent (a) and vortexed (c) conditions appeared as homogeneous solutions below the CC (0.3 mM; left column), while aeration (e) induces tube growth together with a large amount of small aggregates that appear to be mostly bundled around the nanotube morphology (see ×2 zoom inserts to left of panel). The 0.3 mM solution with permanent HHI (g) produced heterogeneous aggregates that are mostly diffuse containing varying degrees of denser sections (see ×3 zoom inserts to left of panel). All solutions above the CC (0.4 mM; right column) assemble into nanotube morphologies. Quiescent conditions above the CC (b) produced a small amount of tube growth together with a similar aggregate morphology to that seen in (e) (see ×2 zoom inserts to right of panel). Vortexing (d), aeration (f), and permanent HHI (h) samples contain nanotubes morphologies only of differing depths. All scale bars 10 µm.

Varying degrees of nucleation and growth are seen in the samples with sub-critical peptide concentrations. As expected, the 0.3 mM quiescent Aβ(16-22):Rh17-22 mixture (Figure 3a) did not assemble below the CC as observed by the homogeneous fluorescence across the entire sample volume. The same homogeneous fluorescence was evident under vortexed conditions below the CC (Figure 3c). In contrast, aeration below the CC (Figure 3e) showed considerable nanotube growth in addition to morphology resembling bundles of aggregated assemblies. Nanotubes are readily identified as long persistence length fluorescent rods with uniform diameter and fluorescence. The bundled assemblies appear jagged with irregular morphologies (Figure 3e; ×2 zoom inserts to left of panel). We estimate that the solution lost by aeration is approximately 10-15% by weight, increasing the 0.3 mM aerated sample to an effective concentration similar to that of the 0.4 mM quiescent conditions (Figure 3b). However, comparison of the aerated sub-CC and supra-CC quiescent samples (Figure 3e compared to Figure 3b) indicates that aeration leads to a greatly increased amount of extended morphologies, and that concentration changes alone cannot explain the enhanced nucleation and growth. The sub-CC solution containing a permanent HHI produced numerous small diffuse aggregates of varying density, with an additional morphology manifesting as spots and clusters of spots (Figure 3g).

Above the CC, all 0.4 mM samples display nanotube morphologies. In addition to the clearly distinguishable homogeneously fluorescent nanotubes, the 0.4 mM sample under quiescent conditions contained a small amount of the bundled aggregate morphologies (Figure 3b; ×2 zoom inserts to right of panel) as seen in the 0.3 mM aerated sample, which are not seen in the remaining 0.4 mM samples. The vortexed and aerated samples (Figure 3d & f respectively) display increasing amounts of nanotube growth. Each image shown is a z-section of the sample approximately 1 µm thick, and thus does not reveal how much of the chamber box well was filled with nanotubes. The arrows on the right side of each image indicate the depth of nanotube mesh network filling the bottom of the chamber box, shown as a relative fraction of the depth of the 0.4 mM aerated sample (Figure 3f). The 0.3 mM aerated and 0.4 mM quiescent samples are shallow enough to fit entirely within a single optical z-section, while the mesh network of the 0.4 mM aerated sample extends approximately 20 µm above the surface. The HHI also significantly increased the amount of nanotube growth at a concentration of 0.4 mM, where the measured mesh of nanotubes extended ~5 µm from the cover glass surface (Figure 3h). Taken together, the introduction of interfaces correlates with a significant increase in nanotube and intermediate assembly; thus allowing for subsequent FLIM analyses of these critical stages of the pathway.

The morphologies that persist using the nucleation methods introduced above can be used to map the pathway(s) from nucleation through final amyloid structure, and to characterize the structural heterogeneity of the intermediate states. To investigate structural aspects of the nucleation pathway(s) we measure the excited state lifetime of the Rh17-22 probe. The fluorescence lifetime, measured using fluorescence lifetime microscopy (FLIM), probes the nano-environment of the Rh17-22 label at different stages of nucleation across the sample. The average fluorescence lifetime of monomeric Rh17-22 in solution is 3.45 ns, identical to the homogeneous fluorescence lifetime of both 0.3 mM quiescent and vortexed samples, suggesting that these solutions are predominantly non-interacting monomers (Figure 4a&b). In comparison, the average fluorescence lifetime of Rh17-22 incorporated into nanotube morphologies is approximately 3 ns, presented as yellow in these FLIM images (Figure 4c & e-h), and the peak at 3 ns in FLIM image histograms (Figure 4i). In addition, the fluorescence lifetime of the bundled aggregates is also reduced (Figure 4c). The reduction in fluorescence lifetime along these jagged elongated assemblies appears heterogeneous, giving an average lifetime ranging from 2.4 to 2.8 ns. The same bundled aggregates can be seen in the 0.4 mM quiescent sample, yet with smaller domain size and a longer average lifetime. FLIM data of diffuse aggregates nucleated using HHIs revealed a fluorescence lifetime of approximately 2.8 ns (Figure 4d), and dense spots with lifetimes as low as 2.5 ns.

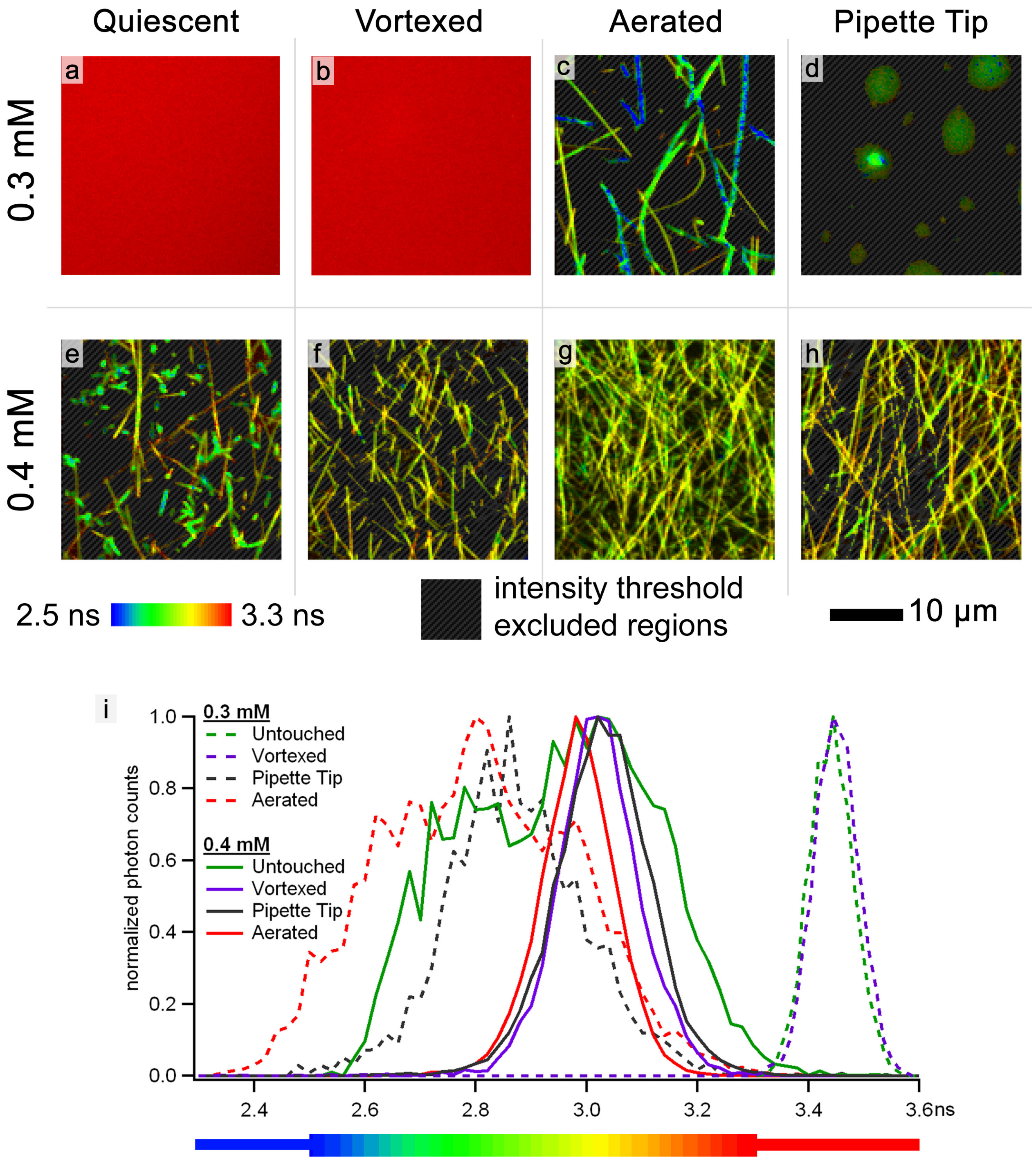

Figure 4 – Fluorescence lifetime imaging microscopy (FLIM) analyses of 0.3 and 0.4 mM aliquots of Aβ(16-22):Rh17-22 assemblies (a-h). Distributions of average fluorescence lifetimes for each image are shown in the histogram (i). Intensity threshold regions (grey striped areas) in images c-h are omitted from corresponding histogram distribution to reduce contribution of background signal from monomer and surface bound peptides. 0.3 mM quiescent (a) and vortexed (b) solutions exhibit average fluorescence lifetimes of 3.45 ns consistent with monomer solutions. 0.3 mM aerated solution (c) contains both 3 ns lifetime nanotubes and bundled aggregate assemblies exhibiting heterogeneous lifetimes ranging from 2.4 to 2.8 ns. Diffuse green aggregates with lifetimes of ~2.8 ns seen in the 0.3 mM pipette tip sample (d) contain small intense spots of shorter lifetime, ~2.6 ns. The above CC 0.4 mM sample in quiescent conditions (e) contains a small amount of nanotubes and bundled aggregates with lifetimes of approximately 2.8 ns. Nanotubes in (e) show regions of longer lifetime, assumed to be a larger contribution from background monomer, either due to being out of focus or incorporation of less Rh17-22 label. 0.4 mM aerated, vortexed and pipette tip containing samples exhibit differing amounts of nanotube growth that have a fluorescence lifetime of approximately 3 ns.

Given that nucleation can be accelerated by the AWI and evaporation, and that the growing globule aggregates can be followed once adhered to the coverslip glass surface, we were able to track the initial stages of nucleated growth using FLIM analysis. Time-lapse FLIM acquisitions reveal an initial fluorescence lifetime for the small aggregates of approximately 2.5 ns (Figure 5a; 0 to 5 hrs). As these aggregates grow in size, short nanotubes appear at the periphery of the aggregate, where the number of growing tubes appears correlated with aggregate size [28]. Concurrent with tube growth, the aggregates experience a reduction in average lifetime from 2.5 to 2.1 ns (Figure 5b), consistent with fluorescence quenching due to a local increase in peptide concentration, corroborating peptide packing and solvent exclusion within the aggregate. Highlighting a ROI containing just nascent tube growth reveals an average fluorescence lifetime with a peak of 2.7 ns (Figure 5c), a fraction lower than mature nanotubes.

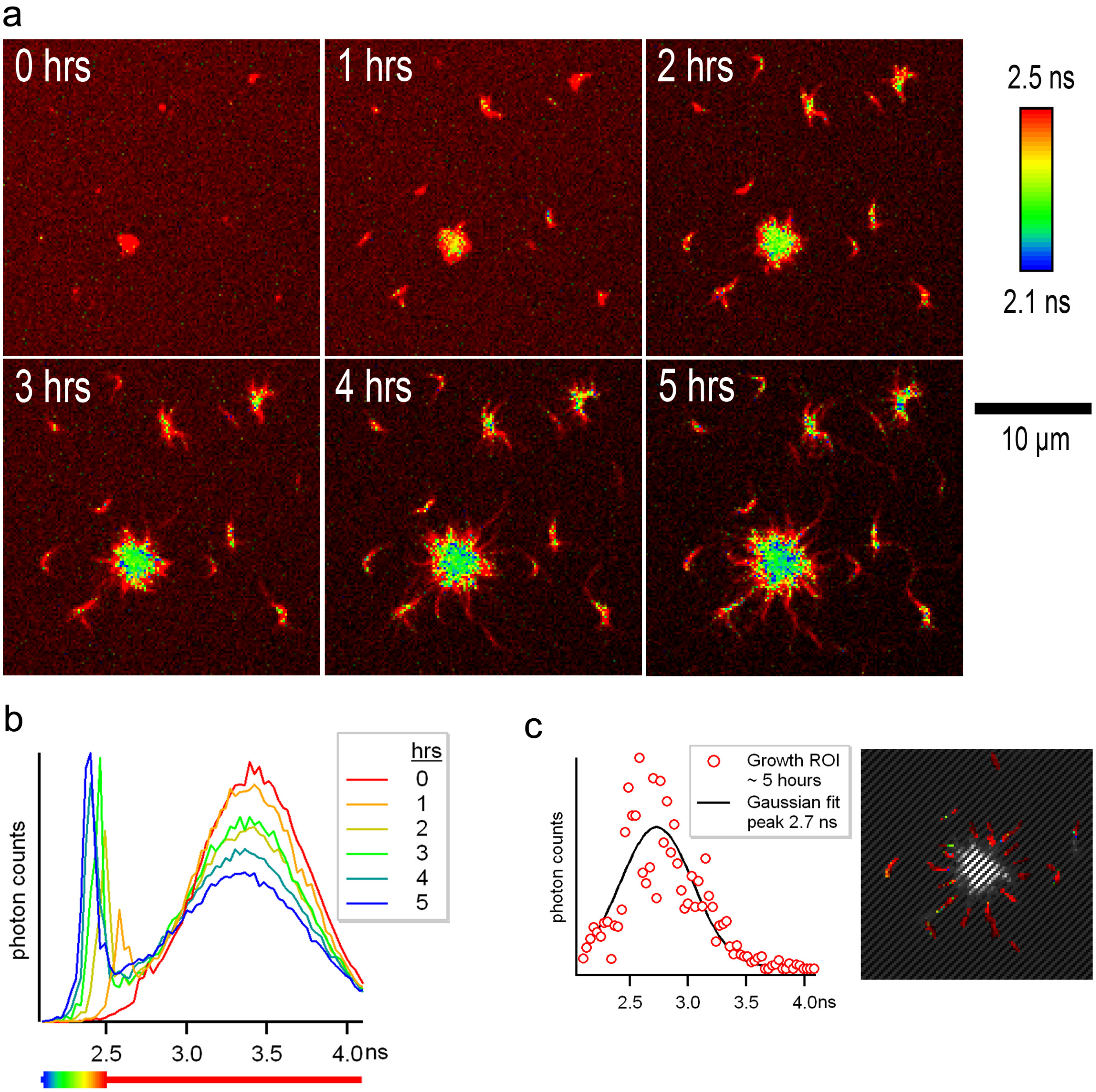

Figure 5 – FLIM analysis of assembly and propagation of aggregate phases at the glass surface. Small aggregates adhered to the surface of the glass observed over time (a) are seen to increase in size and serve as the epicentre of growing tubes. The increase in size is correlated with the amount of growth and a decrease in fluorescence lifetime. FLIM histograms of each time step (b) show a rise in the peak ~ 2 ns, and a decrease in the broad peak ~ 3.5 ns which originates from solution and randomly adhered monomers. Highlighted new tube growth ROI at 5 hours shows nascent growth lifetime of approximately 2.7 ns (c).

The dramatically accelerated nucleation seen immediately following the air-loading procedure (Figure 1), and deposits observed on surveying these samples, motivated our attempts to follow the solution loading in real time. Rh17-22 deposits suspected to be evidence of previous AWIs were observed in the vicinity of growing aggregates (Figure 6a). To gain additional perspective on where these aggregate nuclei might form, slides were prepared using the air-loading process and AWIs were followed using an EMCCD camera. After applying solution to the slide, the fluorescence was uniform across the sample (Figure 6b, panel 1). Following addition of the coverslip, AWIs formed at bubbles and deposits were most obvious along the air escape pathways that appear as streaks of fluorescence (Figure 6b, red arrow). During the AWI collapse, small aggregates are consistently observed in flowing solution (Figure 6b, yellow arrows).

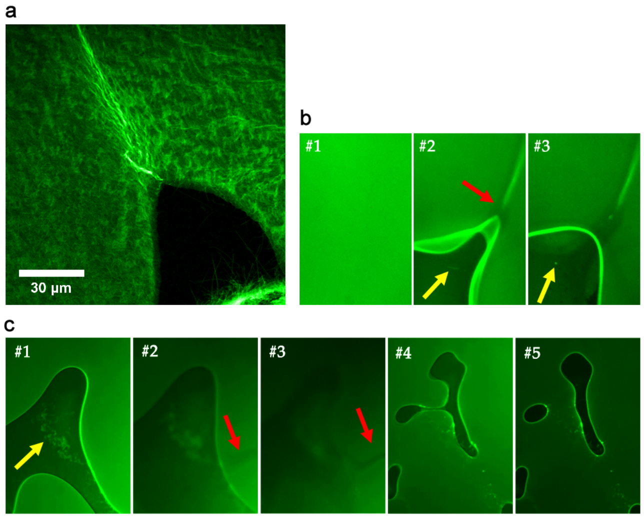

Figure 6 – Capturing the possible origins of nucleating phases during the air-loading protocol. The localities of molten globule aggregates are repeatedly found near remnants of previous AWIs (a). Capturing the behaviour of these compressed bubbles as they form (b) and change (c) reveals aggregates both at AWIs and on the glass surface. The initial air-loading (b, panel 1) and subsequent coverslip addition (b, panels 2 & 3; ESI Mov 1) show the formation of tracks where escaping air movement deposits peptide on the glass surfaces (b, red arrow). Initial bubble collapses are frequently accompanied by aggregates flowing in solution (b, yellow arrows). Thin-film aggregates captured at glass interfaces in air regions appear mobile (c, yellow arrow; ESI Mov 3). Compression, post loading, forces air to escape (c, red arrows), displacing thin-film aggregates to newly formed AWIs and glass interfaces (c, panels 4 & 5).

In addition to AWIs, the glass surfaces are further locations of peptide interactions. Thin film interactions between the glass surface and the trapped air regions appear dynamic (see ESI Mov 1 & 4). A slowly moving collection of fluorescent aggregates can be seen in the trapped air-region in Figure 6c (yellow arrow) that subsequently attach to the periphery of trapped air-region seen in panels 4 & 5. Applying pressure to the upper coverslip, during Figure 6c panels 2 & 3, forces air to exit to the right hand side of the frame (Figure 6c, red arrows). The remaining air-region then settles (Figure 6c, panels 4 & 5), separating into multiple regions. During this process the thin-film region of aggregates has been displaced, sequestered by the AWIs, and deposited on the glass surface in solution. Taken together, these data suggest that nucleating phases originate from a combination of numerous interface interactions and changes in solubility. This observation likely explains the mechanism by which nucleation is enhanced by solvent evaporation in the presence of peptide, but that solvent evaporation prior to dissolving the peptide does not result in similarly enhanced nucleation. In particular, it seems likely that the thin film of peptide solution along the sides of the micro-centrifuge tube, left behind by the evaporating fluid, experiences similar dynamics and nucleation behaviour to that observed in Figure 6.

Discussion

Numerous studies have implicated interfaces in amyloid nucleation [44-46, 49, 53-55]. These earliest phase transitions in amyloid assembly have been correlated with cellular toxicity [11, 56, 57], as on and off the nucleation pathway [4, 6-14], and certainly as short lived and hard to detect intermediates. Accordingly, we sought a simplified system to recreate, image, and characterize the nucleation of cross-β assemblies using interfaces. The nucleating core of the Aβ peptide of Alzheimer's disease, Aβ(16-22), provides a simple model peptide where the thermodynamic assemblies are structurally well defined [58]. Rhodamine-containing probes have also been developed as robust fluorescence reporters of assembly [24]. Here, using numerous interfaces, we have mapped the environmental responsiveness of Aβ(16-22) assembly, from monomer to paracrystalline nanotube.

Using peptide solutions below and above the CC, we have utilized the role of interfaces to access multiple stages of nanotube growth, including suspected transient intermediate structures (Figure 3b,e&g; Figure 4c,d&e). The combination of aeration, together with the small reduction in solubility, clearly leads to a large amount of nucleation above the CC and many aggregates seen adhered to nanotube structures below the CC (Figure 4c). These aggregates are thought to be on-pathway, corroborated by the thick mesh of tube growth, and the absence of aggregates, seen in the 0.4 mM aerated sample (Figure 4g). The constantly present HHI provides a small perturbation from the below CC monomer solution, seen as diffuse aggregates (Figure 4d), not seen in either the quiescent or vortexed conditions. Vortexing did appear to assist nucleation enough to transition the smaller aggregates of the quiescence sample into tube growth, another reason to suspect these aggregates are on-pathway. Taken together, we assign the order of nucleation propensity for the protocol used, from low to high, as: Quiescent, Vortexed, HHI, and Aerated.

The accelerated growth shown in
Figure 1 may be in part due to the large amounts of AWI present during the loading protocol. An additional factor that may play a significant role in directing the nucleation pathway is seen in the remnants of compression and exit tracks of trapped bubbles during loading. Real time capture of these AWIs forming during slide loading corroborates the association of the AWI with nucleation (Figure 6). Inspection of the numerous trapped air-regions during the air-loading protocol revealed that, in addition to peptide interactions at the AWI, mobile thin film aggregates are also present (see ESI

movies). These ‘rafts’ of peptide aggregates are analogous to the 2D diffusion characterized by Shen et al. [53], where weakly adhered peptide surface diffusion was seen as a critical precursor for nucleation, and are observed to transition from thin-film to AWIs during air-region displacement. We conjecture that thin-film and AWI aggregates contain the same nucleating phases observed within growing globules.

Dramatic changes in the AWI topology during rapid bubble collapse and escape trajectories seen during the sample loading protocol are likely occurring during solution aeration as bubbles form at the pipette tip and collapse at the surface. During formation, bubble ‘pinch-off’ at the pipette tip end can lead to dramatic topological fluctuations [59], micron-sized satellite bubbles [59], and rupturing of the trailing bubble edge as it leaves the pipette tip [60]. Conversely, at the end of the bubbles’ lifespan, the small scale violent nature of bubble collapse can lead to sharp increases in local pressure and interface concentrations at the bulk AWI surface. In addition to the possible transfer to the bulk solution AWI *via* bubble flow, peptide-peptide interactions may be occurring at the dynamic bubble AWI during bubble formation and collapse. These results are pertinent to almost all experimentalists that encounter AWIs when investigating hydrophobic, hydrophilic, amphiphilic or polar molecules. The further understanding of interfaces present during sample preparation and loading may provide insight into the broad range of subtlety differing results seen in amyloid research.

We have also begun to characterize the effects of the different introduced interfaces *via* comparison of fluorescence lifetimes with identifiable morphologies of previously determined structures: nanotubes [58] and globules [24]. Assessing FLIM data throughout the different stages of the nucleation pathway, and inferring the mechanism of fluorescence quenching, we map out pathway stages in terms of fluorescence lifetime values. Figure 7 summarizes the above FLIM data with a proposed mapping between inferred structures and measured fluorescence lifetimes. Monomer solutions consistently exhibit a lifetime of 3.45 ns (Figure 7a), and as the peptide density increases with hydrophobic collapse (driven by any combination of concentration, time, interfaces, or solubility) we observe a decrease in the fluorescence lifetime value (Figure 7a-d). The reduced lifetime of observed diffuse aggregates containing punctate regions of higher density with shorter lifetime corroborate this collapse into nuclei (Figure 7c). This density-increase lifetime-decrease continues until a high-density, low-lifetime nucleating phase is formed (<2 ns; Figure 7d), which appears to be similar to the liquid-liquid phases reported previously [28]. The reduction in fluorescence lifetime during these initial hydrophobic collapse stages is presumed to result from de-solvation leading to increased random inter-molecule quenching. Recapturing nucleating aggregates at glass interfaces, we observe a concurrent decrease in fluorescence lifetime on the increase in aggregate size and eventual emergence of nascent nanotube growth (Figure 5). From these minima in lifetime values, the formation of ordered cross-β structure marks the return to longer lifetimes (Figure 7d-f). Bundled aggregate morphologies (Figure 7e) are presumed to contain the nuclei required for tube growth, with an increase in fluorescence lifetime due to an increase in ordered peptide that returns the rhodamine reporter to a more solvated environment. The greatest amount of peptide order and rhodamine solvation terminates with nanotube structures having a lifetime of 3 ns (Figure 7f).

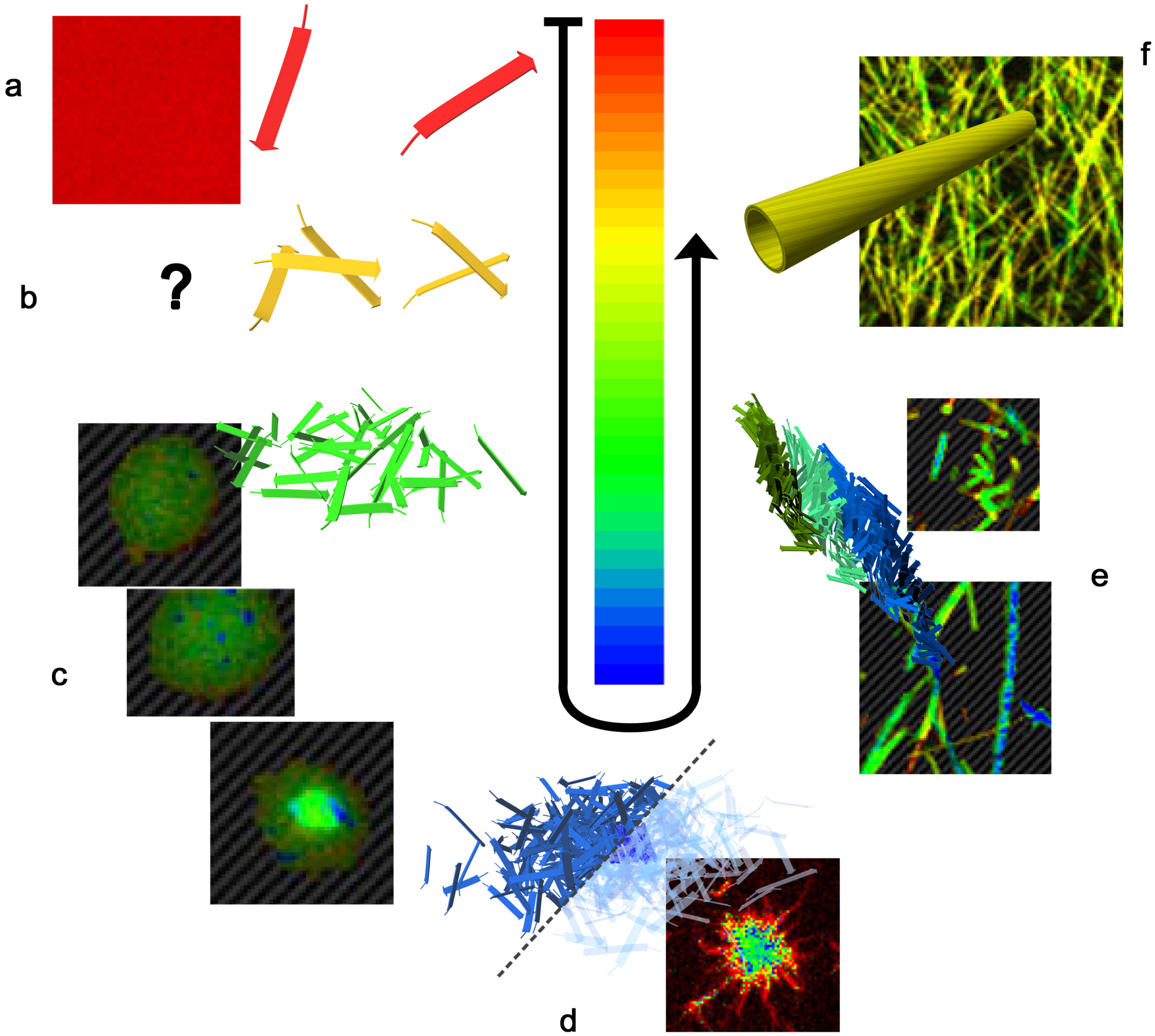

Figure 7 – Proposed mapping of nucleation pathway using fluorescence lifetime and morphology. Monomer solutions (a; red) hydrophobically collapse into dense solvent excluding aggregates that harbour conditions for nucleation (a-d). The initial dimerization is not observable, but inferred (b; orange [down]). Diffuse aggregates begin to exclude solvent (c; green [down]) and show punctate blue regions. High density collapsed molten globules exhibit nucleation (d; blue [minima]). Right-hand side of dashed line shows transparent peptide to highlight nuclei formation within dense aggregate. Bundled nuclei (e; blue/green [up]) increase in order, slowly exposing Rh17-22 to the solvent. Nanotube thermodynamic minima (f; yellow [up]) marks the end point of peptide order and Rh17-22 solvation.

Experimental

Peptide Synthesis

Peptides were synthesized using an Applied Biosystems ABI431 FMOC solid phase synthesizer following standard protocols as outlined in the manuscript. Peptides were cleaved from the resin using trifluoroacetic acid/thioanisole/1,2-ethanedithiol/anisole (90:5:3 2, v/v/v/v), precipitated from the cleavage solution and washed repeatedly using excess cold (-20°C) diethyl ether. Purification was performed using reverse phase HPLC with acetonitrile/water gradients containing 0.1% TFA, and the collected samples were lyophilized to white powder and stored at 4°C. Molecular weights of all peptides were verified by MALDI-TOF mass spectrometry using a 2,5-dihydroxybenzoic acid matrix. Aß(17-22) N-terminal acylated with rhodamine 110 (Rh17-22) were synthesized using the same FMOC and coupling protocols.

Sample Preparation

Small amounts of dry peptide (1-2 mg), weighed in the microfuge tube to an accuracy of ~50 µg, were disaggregated in hexafluoroisopropanol (HFIP). This solution was aliquoted into ~10 new microfuge tubes, and allowed to evaporate in a fume hood before re-entering storage at 4ºC. On use, each aliquot was dissolved in Rh1722 in 40% acetonitrile (MeCN) 0.1% TFA solution to give the required total peptide concentration, followed by alternating sonication and vortexing to ensure complete dissolution. Concentrations of Rh17-22 solutions were verified by absorption using a molar extinction coefficient of 81000 $cm^{-1}M^{-1}$ at 498 nm.

Aeration of the 0.04 mM Aß(16-22)/Rh17-22 solutions (Figure 2) was performed approximately every 12 hours for 1 week, followed by every 24 hours for the subsequent week. Aeration constituted 50 pipettor plunges using a pipettor set to 200 µl with an Eppendorf 2-200 µl epT.I.P.S. tip inserted close to the bottom of the microcentrifuge tube.

Aeration and vortexing of the 0.4 and 0.3 mM Aß(16-22)/Rh17-22 solutions (Figure 3) were performed every day, for four days, followed by three instances of every 2nd day, and finally 2 instances of every 4th day. Samples were left for total of 1 month after dissolving before imaging. Here, aeration constituted 10 plunges of 200 µl as above.

Fluorescence Imaging

Two-photon excitation was provided by an ultrafast (~100 fs pulses at 80 MHz) Ti:Sa laser (Spectra Physics, Santa Clara, CA) tuned to 780 nm, from which the intensity was attenuated using a λ/2 plate and polarizing cube. The laser beam was scanned using an x-y pair of galvanometer mirrors (6215H, Cambridge Technology, Lexington, MA) before entering a 5× beam expanding telescopic optical setup that terminates on the rear aperture of an Olympus 60× water immersion objective lens (UPLSAPO60XW, Olympus, Melville, NY; NA = 1.2) mounted in an inverted microscope (IX71, Olympus, Melville, NY). Introduction into the optical path of the objective was achieved *via* reflection from a dichroic mirror (675 DCSX, Chroma Technology, Brattleboro, VT). The epifluorescent-collected light passes the dichroic mirror and a low pass filter before impinging one of two PMT detector options (H7421-40 for intensity images, and H7422P-40 for FLIM, Hamamatsu Corporation, Bridgewater, NJ). Detector signals were sent to a custom laser scanning acquisition platform (Visμm) for intensity measurements, or a TCSPC module (PicoHarp300, PicoQuant GmbH, Germany), analysed using SymPhoTime software, for FLIM.

Each fluorescence intensity acquisition consisted of one frame at 256×256 pixels with dimensions 50×50 μm and a pixel dwell time of 0.2 ms. Depth measurements were approximate and indicated by the z-translation of the stage controller (MS2000, Applied Scientific Instrumentation, Eugene, OR; Figure 3). FLIM acquisitions consisted of 8 frames at 128×128 pixels with dimensions 30×30 μm and a pixel dwell time of 0.5 ms. The excitation power at the sample was 2 mW, and the images were acquired approximately 2 μm below the glass surface. Reported fluorescence lifetime values were achieved using PicoQuant's 'fastFLIM', which measures the barycentre of the exponential decay, and as such are approximate values with a variance ~0.1 ns. Grey 45° striped areas in FLIM images (Figure 4) indicate regions not included in FLIM histograms to emphasize morphologies over background solution.

In Situ Sample Loading Video

Samples were loaded onto a 22 × 50 mm #1.5 coverslip in custom holder and enclosed with a 22 × 30 mm coverslip. Excitation was provided using an X-Cite 120 (Lumen Dynamics, Canada), using a standard eGFP filter set. Collected movie frames were recorded using an iXon EMCCD camera (Andor, CT) at 30 frames per second.

Conclusions

The data presented here verify the importance of interfaces in the nucleation of Aß(16-22) nanotubes. Using aeration, vortexing and hydrophobic plastic surfaces, we have provided a snapshot of the Aß(16-22) nucleation pathway. Using FLIM analysis, we have begun mapping this pathway in terms of fluorescence lifetimes and peptide morphologies. The corresponding nucleation-lifetime-morphology map has been verified using time-lapse FLIM data of nucleating aggregates. In addition, we have investigated some subtleties of sample loading protocols that lead to considerably accelerated nucleation. Taken together, these data highlight the importance of interfaces in nucleation, and the potential benefits of FLIM analysis for investigations of the dynamics of peptide aggregation. We are now positioned to extend these methods to the larger disease relevant peptides and into the more complex environments associated with disease etiology and functional nano-materials applications.

Acknowledgments

This work has been supported by NSF grant DMR0907435NSF and NASA astrobiology Program, under the NSF Center for Chemical Evolution CHE-1004560 for development of peptide congeners and by the Division of Chemical Sciences, Geosciences, and Biosciences, Office of Basic Energy Sciences of the U.S. Department of Energy through Grant DE-ER15377 for structural analyses. We also thank Dr. Yan Liang for her advice on sample preparation in recreating previous work.

References

1. D. J. Selkoe, *Science*, 2012, **337**, 1488-1492.
2. D. Eisenberg and M. Jucker, *Cell*, 2012, **148**, 1188-1203.
3. I. Benilova, E. Karran and B. De Strooper, *Nature Neuroscience*, 2012, **15**, 349-357.
4. D. M. Walsh and D. J. Selkoe, *Journal of Neurochemistry*, 2007, **101**, 1172-1184.
5. F. Chiti and C. M. Dobson, in *Annual Review of Biochemistry*, 2006, vol. 75, pp. 333-366.
6. M. Stefani, *Progress in Neurobiology*, 2012, **99**, 226-245.
7. W. S. Gosal, I. J. Morten, E. W. Hewitt, D. A. Smith, N. H. Thomson and S. E. Radford, *J Mol Biol*, 2005, **351**, 850-864.
8. A. M. Smith, T. R. Jahn, A. E. Ashcroft and S. E. Radford, *Journal of Molecular Biology*, 2006, **364**, 9-19.
9. R. Kodali and R. Wetzel, *Current Opinion in Structural Biology*, 2007, **17**, 48-57.
10. M. Necula, R. Kayed, S. Milton and C. G. Glabe, *Journal of Biological Chemistry*, 2007, **282**, 10311-10324.
11. M. E. Larson and S. E. Lesne, *Journal of Neurochemistry*, 2012, **120**, 125-139.
12. B. Caughey and P. T. Lansbury, *Annual Review of Neuroscience*, 2003, **26**, 267-298.
13. A. Laganowsky, C. Liu, M. R. Sawaya, J. P. Whitelegge, J. Park, M. Zhao, A. Pensalfini, A. B. Soriaga, M. Landau, P. K. Teng, D. Cascio, C. Glabe and D. Eisenberg, *Science*, 2012, **335**, 1228-1231.
14. M. D. Kirkitadze, G. Bitan and D. B. Teplow, *Journal of Neuroscience Research*, 2002, **69**, 567-577.
15. I. T. S. Li and G. C. Walker, *Proceedings of the National Academy of Sciences*, 2011, **108**, 16527-16532.
16. S. Tanizaki, J. Clifford, B. D. Connelly and M. Feig, *Biophys J*, 2008, **94**, 747-759.
17. A. Fernández, *Physics Letters A*, 2002, **299**, 217-220.

18. I. Daidone, M. B. Ulmschneider, A. Di Nola, A. Amadei and J. C. Smith, *Proc Natl Acad Sci U S A*, 2007, **104**, 15230-15235.
19. B. J. Berne, J. D. Weeks and R. Zhou, *Annu Rev Phys Chem*, 2009, **60**, 85-103.
20. M. G. Krone, L. Hua, P. Soto, R. Zhou, B. J. Berne and J. E. Shea, *Journal of the American Chemical Society*, 2008, **130**, 11066-11072.
21. M. Cheon, I. Chang, S. Mohanty, L. M. Luheshi, C. M. Dobson, M. Vendruscolo and G. Favrin, *Plos Computational Biology*, 2007, **3**, e173.
22. W. Hwang, S. Zhang, R. D. Kamm and M. Karplus, *Proceedings of the National Academy of Sciences of the United States of America*, 2004, **101**, 12916-12921.
23. I. Brovchenko, R. R. Burri, A. Krukau and A. Oleinikova, *Physical chemistry chemical physics : PCCP*, 2009, **11**, 5035-5040.
24. Y. Liang, D. G. Lynn and K. M. Berland, *J. Am. Chem. Soc.*, 2010, **132**, 6306-6308.
25. G. Plakoutsi, F. Bemporad, M. Calamai, N. Taddei, C. M. Dobson and F. Chiti, *Journal of Molecular Biology*, 2005, **351**, 910-922.
26. N. Carulla, M. Zhou, M. Arimon, M. Gairí, E. Giralt, C. Robinson and C. Dobson, *Proceedings of the National Academy of Sciences*, 2009, **106**, 7828-7833.
27. R. Bader, R. Bamford, J. Zurdo, B. F. Luisi and C. M. Dobson, *Journal of Molecular Biology*, 2006, **356**, 189-208.
28. W. S. Childers, N. R. Anthony, A. K. Mehta, K. M. Berland and D. G. Lynn, *Langmuir*, 2012, **28**, 6386-6395.
29. A. M. Morris, M. A. Watzky and R. G. Finke, *Biochim. Biophys. Acta*, 2009, **1794**, 375-397.
30. S. I. A. Cohen, M. Vendruscolo, C. M. Dobson and T. P. J. Knowles, *Journal of Molecular Biology*, 2012, **421**, 160-171.
31. D. Jiang, K. L. Dinh, T. C. Ruthenburg, Y. Zhang, L. Su, D. P. Land and F. Zhou, *Journal of Physical Chemistry B*, 2009, **113**, 3160-3168.
32. L. Jean, Chiu F. Lee and David J. Vaux, *Biophys J*, 2012, **102**, 1154-1162.

33. E. Y. Chi, S. L. Frey, A. Winans, K. L. H. Lam, K. Kjaer, J. Majewski and K. Y. C. Lee, *Biophys J*, 2010, **98**, 2299-2308.

34. G. R. Szilvay, A. Paananen, K. Laurikainen, E. Vuorimaa, H. Lemmetyinen, J. Peltonen and M. B. Linder, *Biochemistry*, 2007, **46**, 2345-2354.

35. D. M. Fowler, A. V. Koulov, W. E. Balch and J. W. Kelly, *Trends Biochem. Sci.*, 2007, **32**, 217-224.

36. I. Macindoe, A. H. Kwan, Q. Ren, V. K. Morris, W. Yang, J. P. Mackay and M. Sunde, *Proceedings of the National Academy of Sciences*, 2012, **109**, E804-E811.

37. M. A. Sani, J. D. Gehman and F. Separovic, *Febs Letters*, 2011, **585**, 749-754.

38. W. Qiang, W.-M. Yau and R. Tycko, *Journal of the American Chemical Society*, 2011, **133**, 4018-4029.

39. A. T. Alexandrescu, S. M. Patil, A. Mehta and S. Jha, *Biochemistry*, 2011, **50**, 2808-2819.

40. M. Bokvist and G. Grobner, *Journal of the American Chemical Society*, 2007, **129**, 14848-+.

41. G. P. Gorbenko, *Journal of Fluorescence*, 2011, **21**, 945-951.

42. C. Schladitz, E. P. Vieira, H. Hermel and H. Möhwald, *Biophys J*, 1999, **77**, 3305-3310.

43. M. Hoernke, J. A. Falenski, C. Schwieger, B. Koksch and G. Brezesinski, *Langmuir*, 2011, **27**, 14218-14231.

44. J. S. Sharp, J. A. Forrest and R. A. L. Jones, *Biochemistry*, 2002, **41**, 15810-15819.

45. D. H. J. Lopes, A. Meister, A. Gohlke, A. Hauser, A. Blume and R. Winter, *Biophys J*, 2007, **93**, 3132-3141.

46. C. F. Lee, S. Bird, M. Shaw, L. Jean and D. J. Vaux, *Journal of Biological Chemistry*, 2012, **287**.

47. L. Munishkina and A. Fink, *Biochimica et Biophysica Acta (BBA) - Biomembranes*, 2007, **1768**, 1862-1885.

48. H. LeVine, 3rd, *Protein Sci.*, 1993, **2**, 404-410.

49. A. Morinaga, K. Hasegawa, R. Nomura, T. Ookoshi, D. Ozawa, Y. Goto, M. Yamada and H. Naiki, *Biochimica et Biophysica Acta (BBA) - Proteins & Proteomics*, 2010, **1804**, 986-995.

50. T. Ban, K. Morigaki, H. Yagi, T. Kawasaki, A. Kobayashi, S. Yuba, H. Naiki and Y. Goto, *Journal of Biological Chemistry*, 2006, **281**, 33677-33683.
51. H. Yagi, T. Ban, K. Morigaki, H. Naiki and Y. Goto, *Biochemistry*, 2007, **46**, 15009-15017.
52. G. Ramachandran and J. B. Udgaonkar, *Journal of Molecular Biology*, 2012, **421**, 296-314.
53. L. Shen, T. Adachi, D. Vanden Bout and X. Y. Zhu, *Journal of the American Chemical Society*, 2012, **134**, 14172-14178.
54. M. R. Nichols, M. A. Moss, D. K. Reed, J. H. Hoh and T. L. Rosenberry, *Microscopy Research and Technique*, 2005, **67**, 164-174.
55. G. Brezesinski, E. Maltseva and H. Möhwald, *Zeitschrift für Physikalische Chemie*, 2007, **221**, 95-111.
56. S. T. Ferreira, M. N. N. Vieira and F. G. De Felice, *Iubmb Life*, 2007, **59**, 332-345.
57. B. Sahoo, S. Nag, P. Sengupta and S. Maiti, *Biophys J*, 2009, **97**, 1454-1460.
58. A. K. Mehta, K. Lu, W. S. Childers, Y. Liang, S. N. Dublin, J. Dong, J. P. Snyder, S. V. Pingali, P. Thiyagarajan and D. G. Lynn, *J. Am. Chem. Soc.*, 2008, **130**, 9829-9835.
59. S. T. Thoroddsen, T. G. Etoh and K. Takehara, *Physics of Fluids*, 2007, **19**.
60. J. C. Burton, R. Waldrep and P. Taborek, *Physical Review Letters*, 2005, **94**.

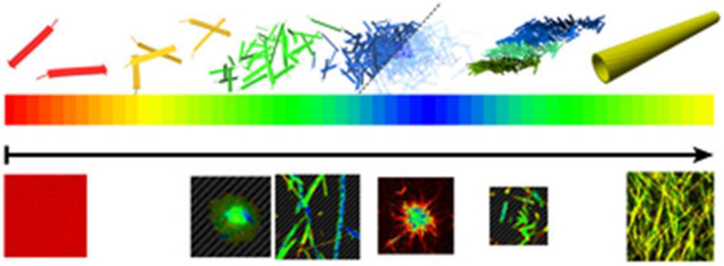

Graphical Abstract
30x12mm (300 x 300 DPI)